Chapter 2
Diaphragm Based Pressure Sensor and System Design

The fiber-optic pressure sensor actually measures displacement caused by the pressure, such as devices utilize diaphragms or bellows as their pressure sensing elements.

Displacement-based fiber optic pressure sensors demonstrated so far can be grouped to four main categories according to how the sensing is accomplished as we mentioned in Chapter 1. These four types of sensors are intensity modulated, wavelength modulated, interferometric or phase modulated and polarization modulated sensors. The question here is which method is suitable to use in our research. Here we look into each type of sensors in more detail.

Intensity-modulated sensors vary the intensity or amplitude of light returned to photodetectors. A typical intensity modulated sensor is the micro-bending sensor, in which the transmitted light is modulated by small bends in a fiber inducing a loss of light at each bend. The amount of loss depends upon the sharpness of the bend. These sensors can be very sensitive to the physical parameter they are measuring. Unfortunately, they are also very sensitive to parameters they are not measuring such as placement and temperature of the transmission cable, and temperature changes in connectors. Carefully constructed systems can probably achieve absolute accuracies approaching 1% in the field.

The second type of sensor is the wavelength-modulated sensor. Bragg gratings are truly wavelength-modulated sensors. The applied pressure associated with the strain will change the grating spacing. One approach is to compress the fiber containing the Bragg gratings. The other approach is to mount the Bragg grating fiber on a pressure sensitive diaphragm. [1]

The third type of sensor is the polarization modulated sensor. This type of sensor modulates the polarization state of the output light according to the physical parameter being measured. Generally, the input light is linearly polarized, either from a special polarization maintaining fiber or a linear polarizer in the transducer. The transducer

then converts some of the light to the orthogonal polarization state. The light in the two orthogonal polarization states is transmitted back to the decoder and decoded as the difference divided by the sum of the intensities. Unless the two polarization states are transmitted back along a true polarization – maintaining single fiber this technique may suffer accuracy limitations that are similar to those of intensity modulated sensors.

The fourth type of sensor is the interferometric sensor. It uses one of several types of interferometers to modulate the optical signal returned to the decoder. Fundamentally, all interferometers operate by modulating the optical path length or phase of part of the optical input with respect to another part. The output of the sensor depends upon the characteristics of the input light, and optical configuration of the interferometer. Generally, the output light consists either of a series of pulses whose position in time depends upon the parameter being sensed, or a wavelength modulated signal.

In an application, which requires an absolute measure of a parameter with high accuracy, it is clear that an intensity-modulated sensor will not suffice. Variations in transmission losses cause too much error in the steady-state measurement. Wavelength modulated sensors can provide high accuracy, but cannot measure dynamic pressure. A polarimetric sensor suffers from the same limitations as an intensity sensor unless special polarization – maintaining fiber is used for the transmission link. For these reasons we have concentrated our efforts on the development of an interferometric sensor system.

We choose to use Fabry-Perot interferometric approach. This sensing scheme has several distinct advantages. Fiber optic sensor based upon the Fabry-Perot interferometer have been shown to provide high sensitivity, 'point' sensing, polarization independence, and multiplexing capacity compared with other interferometric sensing schemes, such as Mach-Zehnder, Michelson or Sagnac configurations.[8] The sensor head is made of fused silica, which provides good temperature stability. Only one fiber is required, which allows the sensor to be compact. The sensor is insensitive to intensity variation in the lead fiber and can be made quite rugged.

2.1 Review of Fabry-Perot Interferometer (FPI)

The Fabry-Perot interferometer (FPI) is a very simple device that relies on the interference of multiple beams. In its simple form, it consists of two parallel, partially transmitting mirrors (semi transparent reflector) that are precisely aligned to form a reflective optical cavity (or called resonator). A monochromatic light wave enters the Fabry-Perot cavity at arbitrary angles and undergoes multiple reflections between the mirrors so that the light can interfere with itself many times. If the frequency of the incident light is such that constructive interference occurs within the Fabry-Perot cavity, the light will be transmitted. A set of bright concentric rings, or fringes is formed on a dark background through a lens. Otherwise destructive interference will not allow any light through the Fabry-Perot cavity. A complementary set of dark fringes is formed on a light background.

If we define the reflectance of a surface as the ratio: [8]

$$R = \frac{reflected}{incident}\frac{energy}{energy} \tag{2-1}$$

and transmittance as the ratio:

$$T = \frac{transmitted}{incident}\frac{energy}{energy} \tag{2-2}$$

The reflectance R is always smaller than 1. We can define a complex coefficient of reflection r if we consider the reflection, no longer in intensity but in amplitude. If ρ is the reflected fraction of the amplitude and φ the phase delay at reflection, we have

$$r = \rho e^{-j\varphi} \tag{2-3}$$

with

$$R = rr^{*} = \rho^{2} \tag{2-4}$$

And if τ is the transmitted fraction of the amplitude and φ', the phase delay introduced in crossing surface or the semi-reflecting film, we define a complex transmission coefficient as

$$t = \tau e^{-j\varphi'} \tag{2-5}$$

with

$$T = tt^* = t^2 \qquad (2\text{-}6)$$

In the case of transparent media r and t are real ($\varphi'=0$ or $\varphi'=\pi$) and we have $r=\rho$, $t=\tau$. All the incident energy reappears in the reflected and transmitted energy. The conservation of the energy permits us to write:

$$R+T=1 \qquad (2\text{-}7)$$

In metallic films, r and t are complex. A fraction L of the energy is lost by absorption. We have

$$R+T+L=1 \qquad (2\text{-}8)$$

In a Fabry- Perot interferometer, a beam of parallel rays with an angle of incidence i is transmitted. To simplify the calculations, we assume that there are two distinct series of rays arrive at point M as shown in Figure 2-1. We also assume that the two surfaces AB and A'B' are identical and the index of refraction n is the same inside and outside the interferometer.

(a) Rays: $a_1, a_2, a_3, \ldots$

(b) Rays: $b_1, b_2, b_3, \ldots$

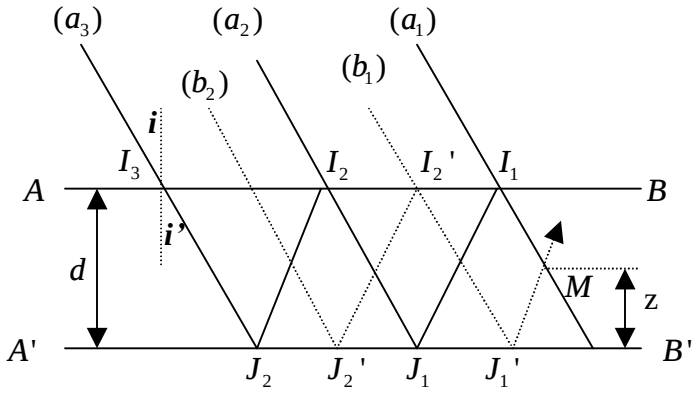

Figure 2-1 Phenomena in the interior of a Fabry-Perot interferometer[8]

The amplitudes of the rays (a) are

Rays: I_1M, $I_2J_1I_1M$, $I_3J_2I_2J_1I_1M$, …

Amplitude: t, tr^2, tr^4, …

The amplitudes of the rays of the series (b) are

Rays: $I_2'J_1'M$, $I_3J_2'I_2'J_1'M$

Amplitudes: tr, tr^3, …

These amplitudes take into account the phase shifts at reflection and transmission by the surfaces AB and A'B'.

The transmitted vibrations corresponding to the rays (a_1), (a_2), (a_3)

$$t,\ tr^2e^{-jj},\ tr^4e^{-j2j},\ \ldots$$

and the transmitted vibrations corresponding to the rays (b_1), (b_2), (b_3)

$$tr,\ tr^3e^{-jj},\ tr^5e^{-j2j},\ \ldots$$

with

$$j = \frac{4p\,nd\cos i}{l} \qquad (2\text{-}9)$$

where d is the thickness of the plate between AB and A'B' and n is its index of refraction.

At point M, the amplitude of the vibration is given by the sum

$$A_a = t + tr^2e^{-jj} + tr^4e^{-j2j} + \ldots \qquad (2\text{-}10)$$

$$A_b = tr + tr^3e^{-jj} + tr^5e^{-j2j} + \ldots$$

Hence for an infinite number of beams we have

$$A_a = \frac{t}{1 - r^2e^{-jj}} \qquad (2\text{-}11)$$

$$A_b = \frac{tr}{1 - r^2e^{-jj}}$$

If φ' is the phase shift at reflection given by Equation (2.3), the intensity in M produced by a rays series is given by

$$I_a = \frac{t}{1-r^2 e^{-jj}} \frac{(t)^*}{1-(r^*)^2 e^{jj}} = \frac{T}{1-2R\cos(j\ +2j\ ')+R^2} \tag{2-12}$$

$$I_b = \frac{tr}{1-r^2 e^{-jj}} \frac{(tr)^*}{1-(r^*)^2 e^{jj}} = \frac{TR}{1-2R\cos(j\ +2j\ ')+R^2}$$

We set

$$f = j\ +2j\ ' \tag{2-13}$$

to obtain

$$1+R^2-2R\cos(f) = (1-R)^2 + 4R\sin^2\frac{f}{2} \tag{2-14}$$

from which

$$I_a = \frac{T}{(1-R)^2}\left[1+\frac{4R}{(1-R)^2}\sin^2\frac{f}{2}\right]^{-1} \tag{2-15}$$

$$I_b = \frac{TR}{(1-R)^2}\left[1+\frac{4R}{(1-R)^2}\sin^2\frac{f}{2}\right]^{-1}$$

The maximum intensity is given by

$$I_{a0} = \frac{T}{(1-R)^2} \tag{2-16}$$

$$I_{b0} = \frac{TR}{(1-R)^2}$$

By choosing

$$F = \frac{4R}{(1-R)^2} \tag{2-17}$$

The rays in M have amplitude of

$$A_a = \frac{t}{1-r^2}\left(1+F\sin^2\frac{f}{2}\right)^{-1/2} \tag{2-18}$$

$$A_b = \frac{tr}{1-r^2}(1+F\sin^2\frac{f}{2})^{-1/2}$$

where F is called the finesse.

The transfer function is given by:

$$I_a / I_{a0} = I_b / I_{b0} = \frac{1}{1 + F \sin^2(f/2)} \quad (2\text{-}19)$$

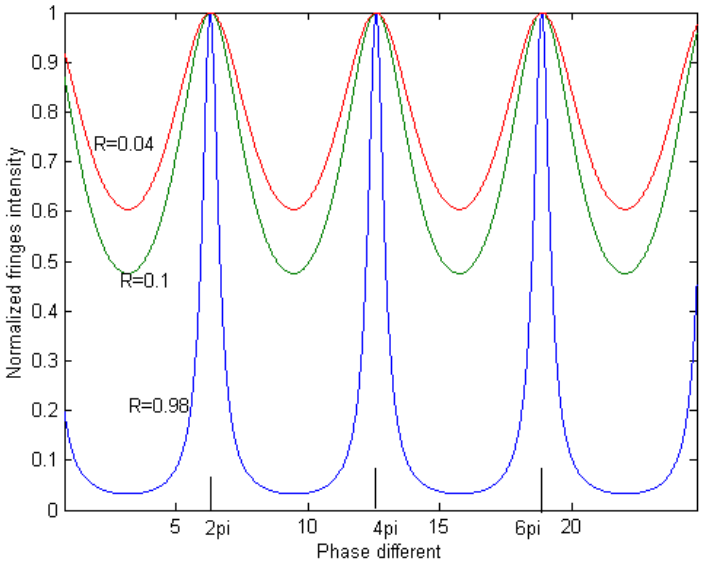

Figure 2-2 Fringes with different reflectance

The phase difference between rays (a) and rays (b) is:

$$y = \frac{4p\, nz \cos i}{l} \quad (2\text{-}21)$$

where z is the distance between M and the plane A'B'. We assume that the inclination *i* of the rays remains small, the vibrations in M are parallel. From Fresnel's classical formula, the intensity in M is

$$I = A_a^{\,2} + A_b^{\,2} + 2A_a A_b \cos y \quad (2\text{-}22)$$

2.2 Principle of Extrinsic Fabry-Perot Interferometric (EFPI) Sensor

Fabry-Perot interferometric sensors can be identified according to the role of optical fiber in sensing process: Intrinsic, in which the perturbation of interest affects the fiber itself; and extrinsic, in which the fiber conducts light to and from a non-fiber sensing element.

We choose to use extrinsic Fabry-Perot interferometer (EFPI) because intrinsic Fabry-Perot interferometer (IFPI) is too sensitive to shield from unwanted external

perturbations. Though its all-fiber design reduces or eliminates the connection problems experienced with EFPI, it usually requires more elaborate signal demodulation. While EFPI sensors are less sensitive and versatile optical fiber sensors, which can be used to measure a wide variety of environment parameters. Due to its unique construction, the EFPI sensor can be configured to measure strain, vibration, temperature, pressure, cure status, or chemical concentration. Using state-of-the art absolute sensing techniques, the EFPI sensor can be made immune to source fluctuations, cable and connector losses, and loss of system power, all of which typically plague intensity-based and differential sensor systems. [10]

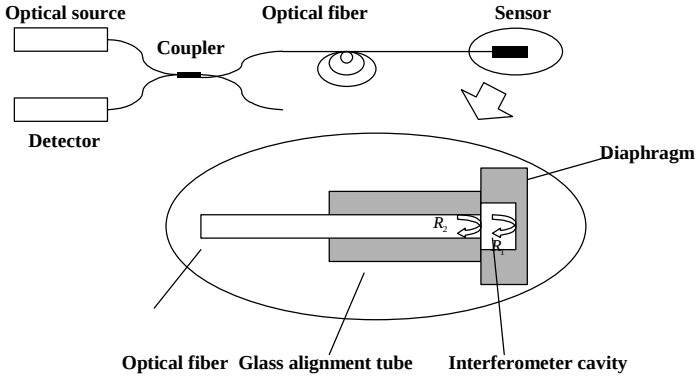

Figure 2-3 Configuration of EFPI Sensor

The configuration of Extrinsic Fabry-Perot Interferometric (EFPI) sensor is shown as Figure 2-3. A single mode silica optical fiber transmits light from a 1550 nm laser diode to the sensor element through a 2x2 coupler. At the sensor head, the laser light signal is partially reflected and partially transmitted across the gap formed by the end of the input fiber and a fused silica diaphragm. The light from the first interface (the input fiber end) and the light reflected at the second interface (the pit on the diaphragm) travel back to a photo-detector where a sinusoidal interference signal can be monitored due to differential phase changes between the two light beams as a result of changes in the EFPI sensor cavity spacing. As we discussed in the section of Fabry-Perot interferometer, the detected photodiode signal current may be shown as the function the phase difference between the two reflected optical fields and is given by:

$$I = A_1^2 + A_2^2 + 2A_1A_2\cos(f_1 - f_2) \qquad (2\text{-}23)$$

where A_1 and A_2 are the amplitudes of the light signals received at the photodetector, and $f_1 - f_2$ is the relative phase difference between the two light signals. If we assume A_1 and A_2 to be equal, equation (2.23) can be rewritten as

$$I = 2I_0\left[1+\cos(\frac{4p\,d}{l})\right] \qquad (2\text{-}24)$$

where d denotes the length of the cavity and λ is the laser diode wavelength of operation in free space.

The simplified relation in Equation (2.24) is sufficient to understand the operation of the EFPI sensor. Changes in the air-gap separation distance between the surfaces of the fiber and the diaphragm produce a sinusoidal modulation of the output intensity signal.

The displacement of the diaphragm by the half of the wavelength changes the path-length difference of the interfering rays by 2π, which corresponds to one period of variation of the radiation intensity at the photo-detector.

Figure 2-4 illustrates the output interference fringes typically obtained from the diaphragm-based EFPI (External F-P interferometer) sensors. An air-gap change of half wavelength can cause the movement of one whole fringe. In principle, continuous tracking of phase changes in the interference fringes can yield information about air-gap changes in the sensor element. The pressure signal causes the deformation of the diaphragm and modulates the sealed air gap length. The sensor therefore gives outputs that correspond to the pressure signals.

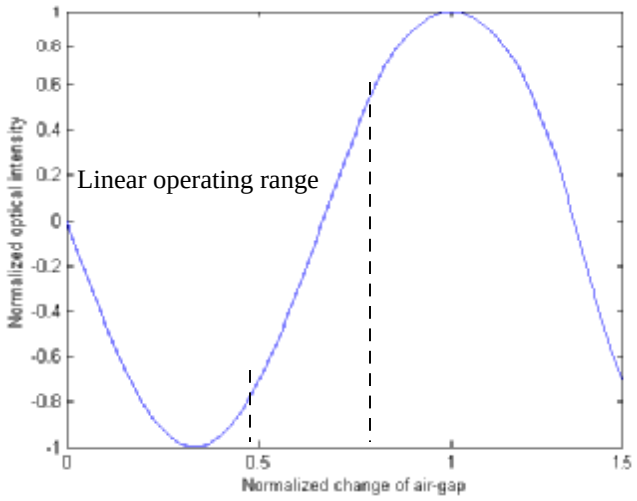

Figure 2-4 Interference fringes of a diaphragm-based EFPI sensor.

Interference Signal

Generally, the intensity of interference rays can be essentially different. In this case 100% visibility of interference can not be achieved even at zero path-length difference of interfering rays.

$$I = I_1 + I_2 + 2\sqrt{I_1 I_2}\cos y \qquad (2\text{-}25)$$

where y is the phase difference of interference rays, I_1 and I_2 are intensities of these two rays.

In an EFPI sensor, as shown in Figure 2-5, $I_1 = RI_0$ is the intensity of the light reflected

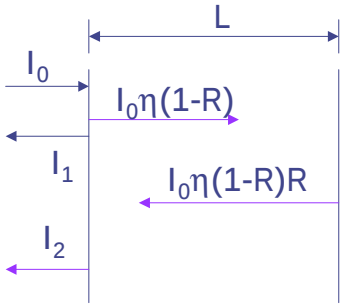

Figure 2-5 Lights reflect/transmitt in an extrinsic Fabry-Perot Interferometer

from the end face surface of the fiber and $I_2 = \eta^2(1\text{-}R)^2 R I_0$ is the intensity of the light reflected from the diaphragm and returned back into the fiber, where I_0 is the intensity of the light incident to the FP cavity, R is the reflectivity of the end face of the fiber and the diaphragm, and η is the coupling coefficient of the Fabry-Perot cavity. For quartz fiber R=0.04 is Fresnel reflectivity of the boundary surface between two substances - glass with refractive index n=1.5 and air with refractive index n=1. Thus, the light intensity detected by a photodetector equals:

$$I = I_0 \times R\left[1 + h^2(1-R)^2 - 2h(1-R)\cos(\frac{4p}{l}L)\right] \qquad (2\text{-}26)$$

Generally, because of divergence of the light at the output of the fiber the percentage of radiation reflected from an external mirror and returned back into the fiber depends upon the distance between the fiber and the diaphragm. [11]

Sensitivity and Linear Range

The quality of the optical interference is described by the parameter- fringe visibility, defined by:

$$g = \frac{I_{\max} - I_{\min}}{I_{\max} + I_{\min}} \qquad (2\text{-}27)$$

where I_{min} and I_{max} are the minimum and maximum intensities of the optical interference, respectively. Obviously, γ depends on η and R.

In our sensor, the pressure signal generated by an engine can cause the deformation of the diaphragm, which modulates the sealed air gap length. The sensor therefore gives outputs that correspond to the pressure signals, as shown in Figure 2-6.

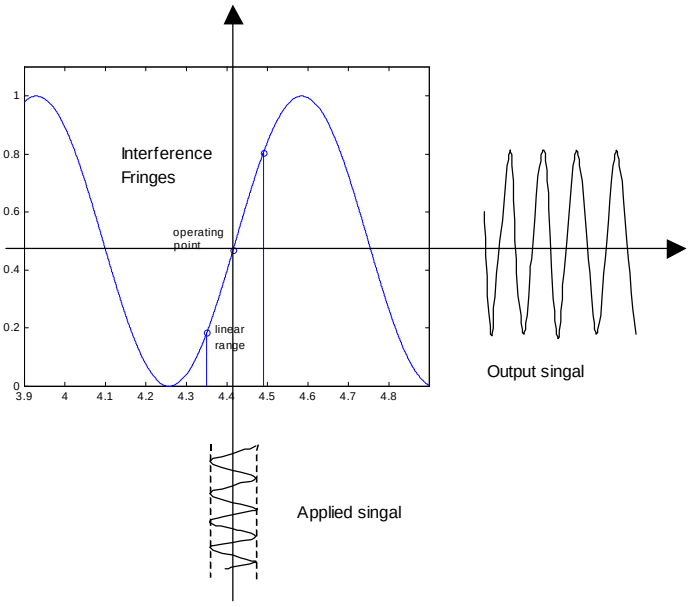

Figure 2-6 Illustration of a linear operating range of the sensor response curve.

The sensitivity of an interferometer (I_{sens}) can be defined as the intensity change produced in response to unit air gap variation,

$$I_{sens} = abs(\frac{dI}{dL}) = abs(b \cdot \frac{4p}{l_c} \sin(\frac{4p}{l_c} L)) \qquad (2\text{-}28)$$

where $b = 2RAI_0\eta$. The maximum sensitivity (I_{sens}(max)) obtained at the quadrature point of the interference fringes is:

$$I_{sens}(\max) = b\,\frac{4p}{l_c} \qquad (2\text{-}29)$$

Like regular interferometers, the measurement will have ultra-high sensitivity. One period of fringe variation corresponds to an air gap change of one-half of the optical wavelength. However, from Equation (2.28), the measurement would suffer from the disadvantages of sensitivity reduction and fringe direction ambiguity when the sensor reaches peaks or valleys of the fringes. Sensitivity is reduced at the peak or valley of a fringe since at that point the change in optical intensity is nearly zero for a small change in the air gap. Fringe direction ambiguity refers to the difficulty in determining whether the air gap is increasing or decreasing by detecting the optical intensity. If a measurement starts with an air gap corresponding to the peak of a fringe, the optical intensity will decrease, regardless of whether the gap increases or decreases. Therefore,

we define the operating range of the sensor ($I_{operating}$ in μm) as its sensitivity remaining within the 60% of the maximum sensitivity.

$$I_{operating} = Solution\{I_{sens} \le b\,\frac{4p}{l} \bullet 60\%\} \qquad (2\text{-}30)$$

Within this range, a pressure induce air-gap change can be realized linearly by the sensor. Obviously, in order to measure precisely the pressure, it is very important to ensure the sensor work within its operating range.

2.3 Self-Calibrated Interferometric/Intensity Based (SCIIB) Fiber Optic Sensor Technology

The self-calibrated interferometric/intensity based (SCIIB) sensor technology is originated from the well-developed extrinsic Fabry-Perot interferometric (EFPI) optical fiber sensors. The self-calibrated interferometric/intensity-based (SCIIB) fiber sensors successfully combine the advantages of both the interferometric and the intensity-based fiber sensors in a single system. [11] The basic idea of the SCIIB system is to have a second channel as reference in addition to the signal channel. This makes it possible to compensate for the source power fluctuations and the fiber loss changes and therefore provide absolute measurement of various parameters.

As shown in Figure 2-7, the reflected light from the sensor head is split into two channels by a splitter. The light in Channel 1 retains its original spectral width (wideband spectrum) while the light in Channel 2 has a much narrower spectrum after passing through an optical band-pass filter. The different spectral widths of the light result in different coherence lengths of these two channels

Assume that the original spectrum width of the source can be approximated as a Gaussian profile with a spectral width of $\Delta\lambda_1$, and also assume that the spectral characteristic of the optical band-pass filter is a Gaussian profile too, but with a different spectral width of $\Delta\lambda_2$. The light spectra seen by the two SCIIB channels can thus be expressed by

$$I_{s1,s2}(l) = \frac{2I_{10,20}}{\sqrt{p}\,\Delta l_{1,2}} \exp(-\frac{(l - l_c)^2}{\Delta l_{1,2}^{\ 2}}) \qquad (2.31)$$

where $I_{10,20}$ are the optical power of two channels respectively, and λc is the central wavelength for both channels.[22]

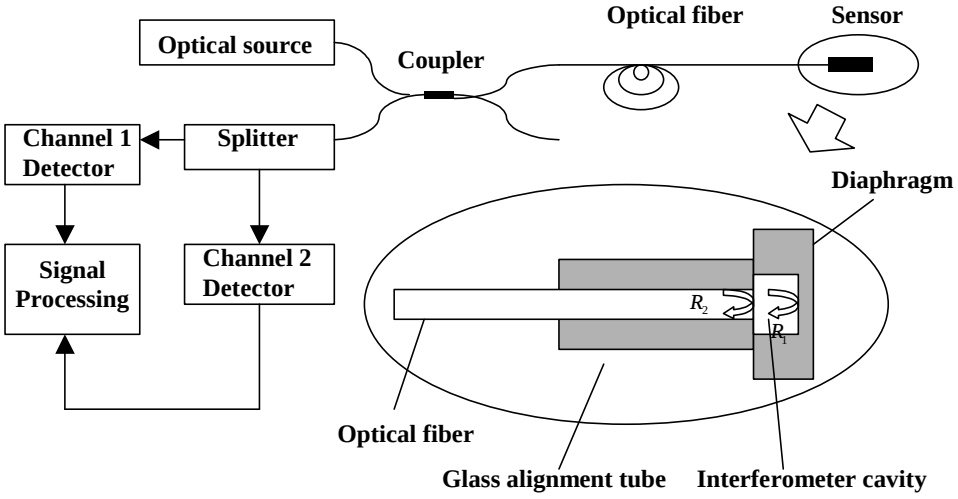

Figure 2-7 Configuration of SCIIB system

The interference signals resulting from the spectra of the two channels can thus be written as

$$I_{1,2} = R \times \int_{-\infty}^{+\infty} I_{s1,s2}(l)\left[1 + h^2(1-R)^2 - 2h(1-R)\cos(\frac{4p}{l}L)\right] d\,l \qquad (2.32)$$

where $I_{s1,s2}$ are the spectral power density distribution of the two channels respectively, R is the reflectance at the boundary of the air and the fiber endface, L is the cavity length. η is the coupling coefficient of the Fabry-Perot cavity. It is a function of cavity length L, the lateral offset, and the angular offset. Because the initial cavity length usually is chosen to be very small, the optical loss of the cavity is very small. Therefore, η cam be approximated to 100%.

The reflectance R can be calculated by

$$R = \left(\frac{n - n'}{n + n'} \right)^2 \tag{2.33}$$

where n is the refractive index of the fiber core, and n' is the refractive index of the medium forming the cavity between two fibers, which in our case is the air. The reflectance at the fiber end face and the diaphragm is the thus about 4% of the total incident optical power.

Since the reflectance is relatively small, the interference signals given by Equation (2.32) can be approximated by

$$I_{1,2} \approx 2R \cdot \int_0^{\infty} I_{s1,s2}(l) \left[1 - \cos\left(\frac{4p}{l} L \right) \right] dl \tag{2.34}$$

By taking the ratio of the two channels outputs, we then have the SCIIB output given by

$$s = \frac{I_2}{I_1} = \frac{\int_{-\infty}^{+\infty} I_{s2}(l) \left[1 + h^2 (1-R)^2 - 2h(1-R) \cos(\frac{4p}{l} L) \right] dl}{\int_{-\infty}^{+\infty} I_{s1}(l) \left[1 + h^2 (1-R)^2 - 2h(1-R) \cos(\frac{4p}{l} L) \right] dl} \tag{2.35}$$

2.4 Diaphragm-based EFPI Pressure Sensor

The geometry of the diaphragm based pressure sensor can be illustrated using Figure 2-8. The interference cavity is formed by wet chemical etching a round pit on the diaphragm. When static and dynamic pressures are applied, the diaphragm will deform, and as the consequence the cavity length will change. By monitoring the sensor cavity length changes through the previously discussed SCIIB signal processing system, the applied pressure can thus be measured.

For a pressure sensor for measurements in engine, the following design criteria are important:

- The pressure sensor must have a high pressure-sensitivity for a sufficient signal to noise ratio in the interesting frequency range.
- The thickness of the pressure sensitive diaphragm must be thick enough in order to withstand high static pressure in engine.
- The diameter of the interference cavity must big enough (But there must be enough space to bond the diaphragm and the tube) in order to test small dynamic pressure.

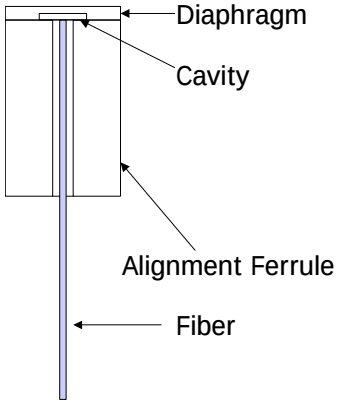

Figure 2-8 Geometry of diaphragm based pressure sensor probe

2.4.1 High temperature design challenge for sensor materials

In my work fused silica was chosen for the pressure-sensitive sensor diaphragm. The main reasons for using fused silica are its inertness and stability at extremely high temperatures; and excellent transparency. In addition, fused silica offers an extremely low coefficient of thermal expansion and high Young's Modulus, which makes it immune to stress effects from thermal shock or thermal gradients. It is widely available, hard and easy to fabricate into specialized components at modest cost. And finally, fused silica remains elastic (no observable creep or hysteresis) up to temperatures very near its annealing point of 1100°C. Thus it is a nearly ideal sensor material. Many of these advantages indicate why fused silica is widely used in microsensor and microacuator technologies of high accuracy.

2.4.2 Diaphragm design

A structure model for a diaphragm is shown in Figure 2-9. *r* is the radius of free area of the diaphragm (In our design, r is the radius of a etched pit on a diaphragm); *h* is the thickness of the diaphragm;

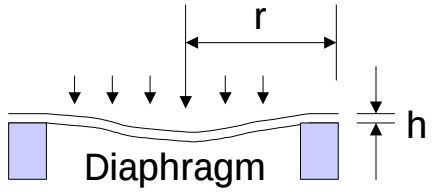

Figure 2-9 Structure model for the diaphragm

Diaphragm Frequency

We define the diaphragm as a free vibrating circular plate cramped at edge. So its natural frequency f_{mn} is given by [14]

$$f_{mn} = \frac{a_{mn}}{2p\,r^2} \times \sqrt{\frac{Dg}{hw}} \qquad (2.36)$$

where α_{mn} is a constant related to the vibrating modes of the diaphragm, listed in Table 2-1; g is the gravitational constant; w is the density of the diaphragm material; D is the flexural rigidity of the diaphragm defined by

$$D = \frac{Eh^3}{12(1-m^2)} \qquad (2.37)$$

where m is the Poisson's ratio; E is the Young's modulus of the fused silica glass material. From the properties of fused silica shown in Table 2-2, the frequency response of the sensor can thus be calculated by combining Equation (2.36) and Equation (2.37)

$$f_{mn} = 2.749 \times 10^9 \times \frac{a_{mn}}{a_{00}} \frac{h}{r^2} \qquad (2.38)$$

where h and r are in microns.

As indicated by Equation (2.38), the sensor's frequency response is proportional to the thickness of the diaphragm and inversely proportional to the square of the effective diaphragm radius.

In order to obtain flat frequency response from DC to 150KHz, let 1000kHz ≥ f_{00} ≥ 500kHz. The maximum usable frequency should be taken to be one fifth or one seventh of its natural frequency. [25] The relationships of frequency response and r and h are given in Figure 2-10.

Table 2-1. Values of α_{mn}

α_{mn}	n = 0	n = 1	n = 2
m = 0	10.21	21.22	34.84
1	39.78	60.82	84.58
2	88.90	120.12	153.76

Table 2-2. Properties of fused silica (@25°C)

Density	$w(r)$	2.202×10^{3}	$Kg\text{-}m^{-3}$
Young's Modulus	E	73.73×10^{9}	Pa
Poisson's Ratio	μ	0.17	-
Max. tensile stress	ρ_m	$\sim 1.5 \times 10^{9}$	Pa
Coefficient of thermal expansion	α_T	$\sim 5.5 \sim 7.5 \times 10^{-7}$	$(\,^{\circ}C)^{-1}$

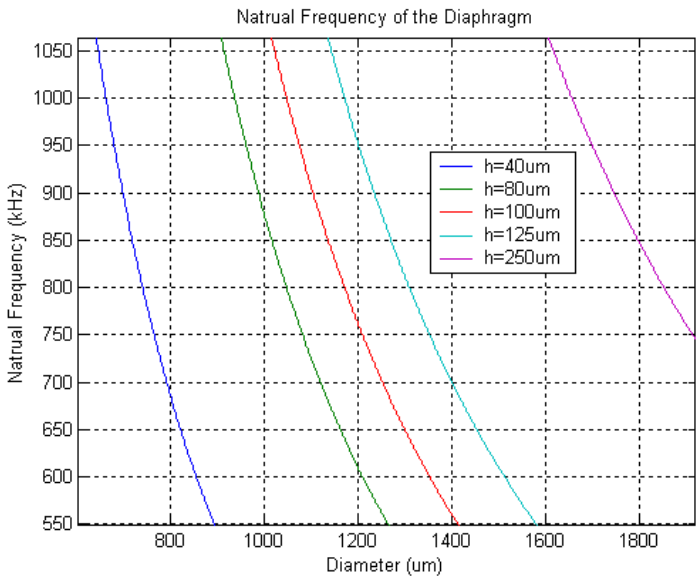

Figure 2-10 Predicted frequency response of the sensor versus cavity diameter

Sensitivity

The diaphragm will be deflected when there is a differential pressure p between the inside and outside of the sealed cavity. The out-of-plane deflection of the diaphragm *y* is a function of the pressure difference at any radius position a. [14]

$$y = \frac{3(1-m^2)p}{16Eh^3} \times (r^2 - a^2) \qquad (2.39)$$

Usually, we define the ratio between the deflection and the pressure difference as the diaphragm sensitivity (δ_{diap}) for pressures. When the fiber is positioned to the center of the diaphragm, only the center deflection y_0 is of interest, so δ_{diap} (for fused silica material) is given by

$$d_{diap} = \frac{y_0}{p} = \frac{3(1-m^2)}{16Eh^3} \times r^4 = 1.71 \times 10^{-8} \frac{r^4}{h^3} \qquad (2.40)$$

where y_0 is in micron, and p is in pound per square inch (psi), so d_{diap} is in μm/psi.

The diaphragm thickness and diameter dependence of the sensitivity is calculated and shown in Figure 2-11.

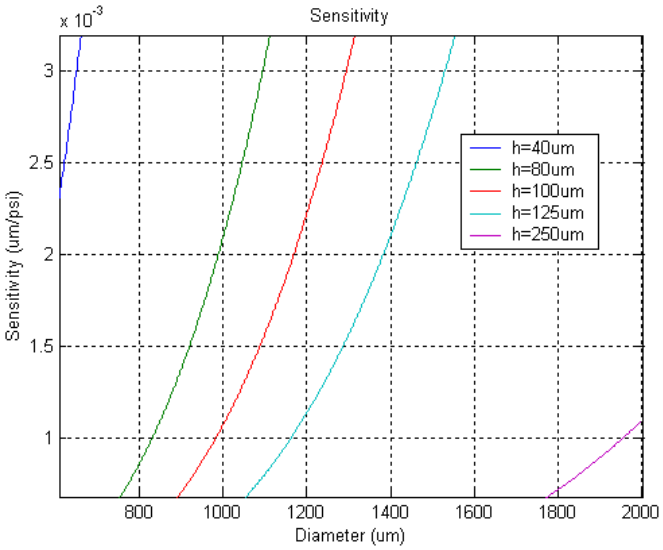

Figure 2-11 Predicted diaphragm sensitivity versus cavity diameter

We considered the frequency response and the diaphragm sensitivity comprehensively and drew conclusions for the thickness of the diaphragm and the diameter of the interference cavity. The sensor should have a pressure sensitive diaphragm with thickness (after wet etch) around 90 μm and an interference cavity on the diaphragm with diameter around 1000 μm.

2.4.3 EFPI pressure sensor

As we analyzed in the previous sections, our sensors are going to use EFPI sensing technology. There are also several other considerations during the design process of the pressure sensor, such as what kind of fibers we should choose and the size of the ferrule.

2.4.3.1 Single mode EFPI sensor

In our research, we decided to fabricate single mode diaphragm-based EFPI sensor. There are several reasons for us to use single mode fiber.

From the view of sensor fabrication, if a multimode fiber is used, there is more than one mode reflected from the diaphragm. If the mode reflected from the diaphragm doesn't activate the original mode, it will affect the interference fringe visibility. This property makes the sensor fabrication more difficult.

From the signal detection standpoint, for a SCIIB system, there is no big difference between the use of single mode and multimode fibers. But single mode fiber components, such as long wavelength filters, are more readily available because of the development of single mode fiber communications.

From the view of measurement capability, light source for single mode fiber system has narrower spectral width. So the single mode fiber system has greater coherence length, which can be seen from equation (2.41). This property provides much more larger dynamic range for pressure testing.

$$L_c \approx \frac{l_c^{\,2}}{\Delta l} \qquad (2.41)$$

where λ_c is the central wavelength of the source and $\Delta\lambda$ is the spectral width of the source.

For future practical use, single mode fiber as a transmission line has less transmission loss compared with multimode fiber. So the sensors made by single mode fiber can be used for long-distance monitor.

2.4.3.2 Alignment Ferrules

In order to obtain good interference signals, the fiber and the diaphragm must be maintained in a good alignment. This requires that the inner diameter (ID) of the feurrle can only be slightly larger than the diameter of fiber cladding (125 μm). Therefore, we choose the inner diameter of the ferrule to be 127 μm.

In order to provide a space for the bonding of the ferrule to the diaphragm, the outer diameter of the ferrule must be greater than 1000 μm. Therefore, we choose the outer diameter of the ferrule to be 1800 μm.

2.5 System structure

The Center for Photonics Technology (CPT) at Virginia Tech developed a SCIIB system for the signal processing of the diaphragm-based pressure sensor. A schematic of the SCIIB system is shown in Figure 2-12. The system is consisted of the following sub-systems:

- A diaphragm based pressure sensor;
- A high power light source system;
- Optical components;
- Two photodiodes and preamplifiers;
- Voltage amplifiers and a analog divider;
- A/D and D/A converters;
- Digital signal processing board;
- Power supply sub-system.

Light Source – High power LED

The light source used in the system is a 1550nm edge-emitting LED(ELED) which can launch a maximum power of 50~60 μW into a single-mode fiber pigtail. The FWHM is about 83nm.

In-line CWDM filter

The filter is working at 1551 nm with a bandwidth of 16.9nm at 0.5dB and 18nm at 3 dB.

From equation (2.35) and

$$\Delta l = \frac{\Delta l_{FWHM}}{\sqrt{2\ln 2}} \qquad (2.41)$$

the system output simulation is shown in Figure 2-13 (a),(b) and (c).

The simulation results show that the coherent ability of the wideband channel is much less than that of narrowband channel. Thus if the airgap is chosen to be around 20 μm,

the wideband signal will keep stable while the narrowband will still see strong interference.

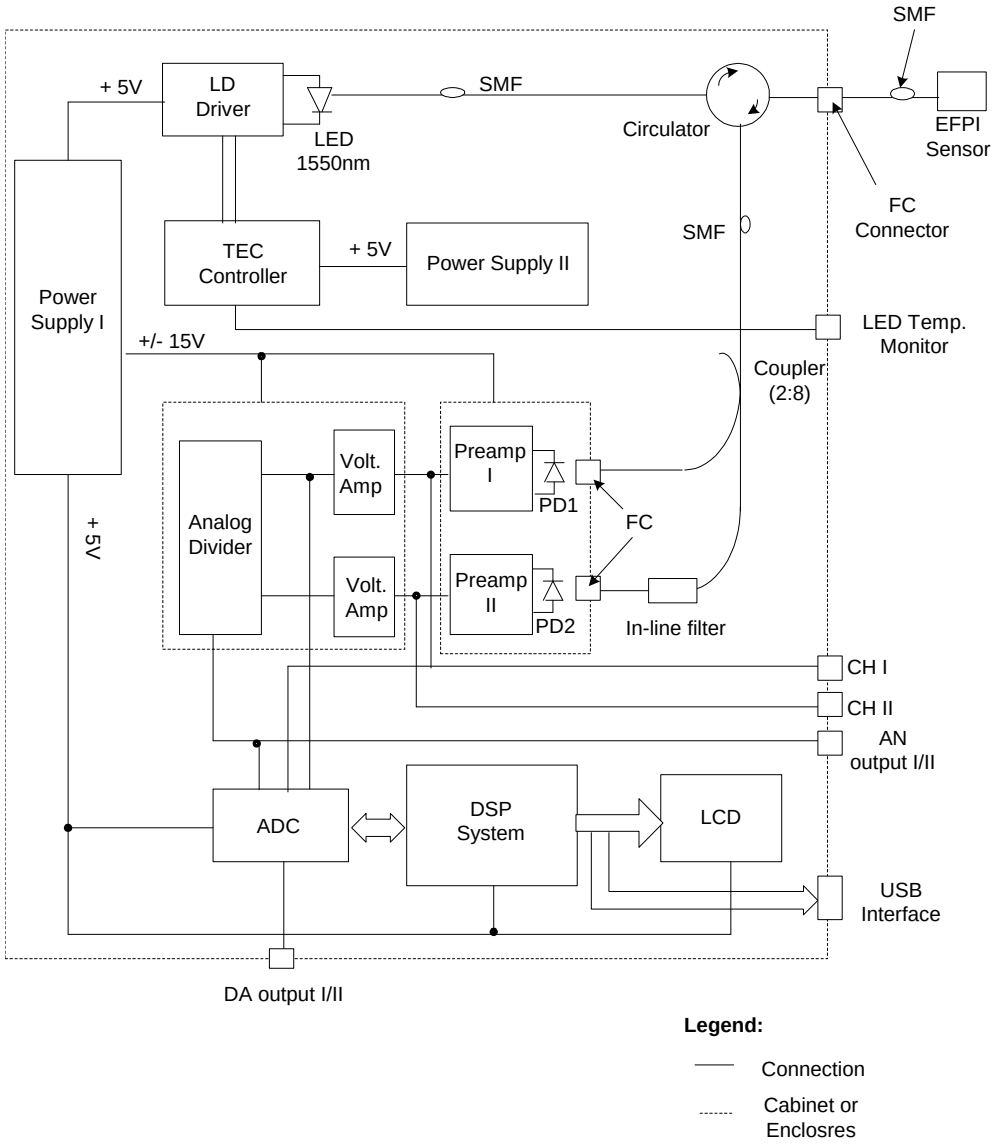

Figure 2-12 A schematic of the diaphragm based engine sensor system

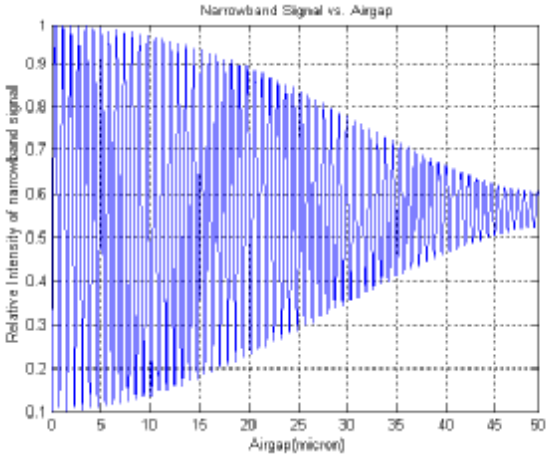

Figure 2-13 (a) SCIIB Narrow-band Output

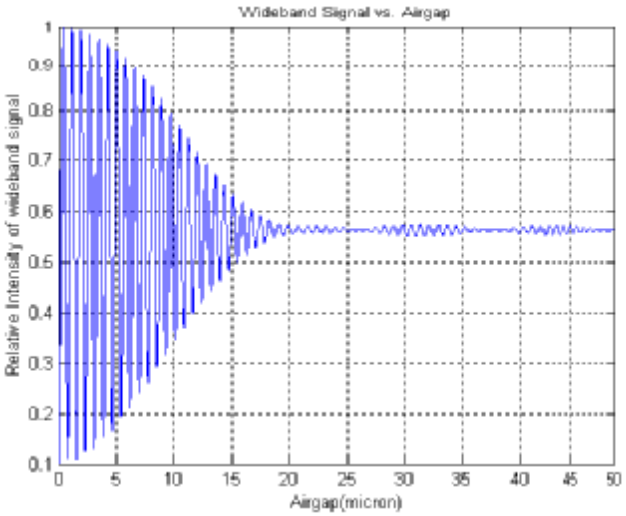

Figure 2-13(b) SCIIB System Wide-band Output

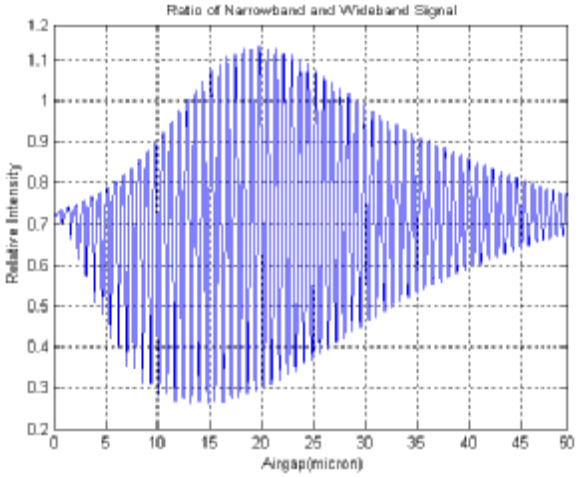

Figure 2-13(c) SCIIB System Output-
Ratio of Narrow-band to Wide-band Output